RSC Advances

PAPER

View Article Online
View Journal | View Issue

Cite this: *RSC Adv.*, 2019, **9**, 37714

The role of cation and anion dopant incorporated into a ZnO electron transporting layer for polymer bulk heterojunction solar cells†

Soyeon Kim,[a] Jaehoon Jeong,[a] Quoc Viet Hoang,[b] Joo Won Han,[c] Adi Prasetio,[ac] Muhammad Jahandar,[a] Yong Hyun Kim,[c] Shinuk Cho*[d] and Dong Chan Lim*[a]

Received 2nd September 2019
Accepted 12th November 2019

DOI: 10.1039/c9ra06974g

rsc.li/rsc-advances

Doping is a widely-implemented strategy for enhancing the inherent electronic properties of charge transport layers in photovoltaic devices. A facile solution-processed zinc oxide (ZnO) and various cation and anion-doped ZnO layers were synthesized *via* the sol–gel method and employed as electron transport layers (ETLs) for inverted polymer solar cells (PSCs). The results indicated that all PSCs with doped ZnO ETLs exhibited better photovoltaic performance compared with the PSCs with a pristine ZnO ETL. By exploring the role of various anion and cation dopants (three compounds with the same Al^{3+} cation: $Al(acac)_3$, $Al(NO_3)_3$, $AlCl_3$ and three compounds with the same Cl^- anion: NH_4Cl, $MgCl_2$, $AlCl_3$), we found that the work function changed to favor electronic extraction only when the Cl anion was involved. In addition, the conductivity of ZnO was enhanced more with the Al^{3+} cation. Therefore, in inverted solar cells, doping with Al^{3+} and Cl^- delivered the best power conversion efficiency (PCE). The maximum PCE of 10.38% was achieved from the device with ZnO doped with Al^+ and Cl^-.

1. Introduction

Bulk heterojunction (BHJ) polymer solar cells (PSCs) have attracted substantial attention for their potential applications in large-area flexible devices due to their unique advantages, such as being inexpensive and easy to fabricate, low weight, and possessing mechanical flexibility.[1–4] After extensive studies on new conjugated polymers and new charge transport interlayers, single-junction PSCs have recently achieved an impressive power conversion efficiency (PCE) of over 15%.[5,6]

In general, according to the hole and electron extraction direction, PSCs are classified as two types, conventional structure PSCs and inverted structure PSCs. Among them, the inverted structure has been preferred recently because it is known that inverted PSCs exhibit better stability.[33,34] The inverted PSCs are basically composed of sequential stacking of the electron transport layer (ETL), photoactive layer, and hole transport layer (HTL) between the transparent indium tin oxide (ITO) and top metal electrode. In these inverted PSCs, since we utilize the ITO as a cathode electrode, a noble metal with a high work function (WF) such as Ag or Au must be used as a top anode electrode. Between Ag and Au, the use of silver is preferred because of its cheap price and easy processability. However, Ag has a similar WF to ITO (WF of ITO ~ 4.7 eV, WF of Ag ~ 4.6 eV). Thus, the inverted PSC with an Ag anode has an insufficient electromotive force for photocurrents. Increasing the potential difference of inverted PSCs is another role of the HTL and ETL layers. Therefore, it is very important that the charge transport layer not only has a good conductivity but also has a proper WF value capable of producing a sufficient driving potential.[7,8,10]

Various metal oxide materials have been utilized as charge transporting functional layers to date. Examples of metal oxide with good electron transport properties include ZnO,[11–15] TiO_x,[16–18] SnO_2,[19–21] and $Zr(acac)_4$.[22,23] Examples metal oxides with good hole transport properties include MoO_x,[15,24–26] V_2O_5,[26–28] NiO_x,[29,30] and WO_x.[31,32] Among ETLs, ZnO has been most widely used due to its high electron mobility, suitable work function, transparency, environmental stability, facile solution processing, low cost, and simple modification.[35,36] In the fabrication of organic solar cells, ZnO is mainly prepared using the sol–gel method. However, wet-chemically prepared ZnO shows relatively low conductivity. In addition, it easily forms trap states associated with defects, which may induce a reduction of the PCE.[35–37]

[a]*Surface Technology Division, Korea Institute of Materials Science (KIMS), 797 Changwondaero, Seongsan-gu, Changwon, Gyeongnam 51508, Republic of Korea. E-mail: dclim@kims.re.kr*

[b]*Vietnam–Korea Technological Innovation Center, Directorate for Standards, Metrology and Quality (STAMEQ), No. 8 Hoang Quoc Viet, Cau Giay, Ha Noi, Vietnam*

[c]*Department of Display Engineering, Pukyong National University, Busan 48513, Republic of Korea*

[d]*Department of Physics, EHSRC, University of Ulsan, Ulsan 44610, Republic of Korea. E-mail: sucho@ulsan.ac.kr*

† Electronic supplementary information (ESI) available: High-resolution XPS spectra, AFM height images, XRD, and UPS spectra. See DOI: 10.1039/c9ra06974g

To achieve higher performance by overcoming both the low conductivity and defect problem, either surface modification or doping with an ionic element have been applied. Several surface modification methods, including the insertion of self-assembled monolayers,[9,38] treatment with either amine or an alcohol polar solvent,[39,40] and the introduction of fullerene-based layers,[41,42] have been employed between the active layer and the ZnO ETL.

However, these methods affect only the surface of a ZnO layer. Thus, the intrinsic opto-electrical properties of ZnO are not substantially improved. As an alternative way to favorably change the properties of the bulk ZnO layer, element doping using aluminum,[43,44] indium,[45] magnesium,[46] chlorine,[47] and hydrogen[48] have been applied, resulting in significantly improved photovoltaic performance and stability by eliminating the defect states.

There are two kinds of vacancy defects in solution-processed ZnO. One is a Zn vacancy, and the other one is an oxygen vacancy. The Zn vacancy can be filled by cation dopants. For example, small radius Al^{3+} ions (0.54 Å) better occupy interstitial sites in a ZnO lattice compared with larger Zn^{2+} ions (0.74 Å).[49–51] On other hand, defects of oxygen vacancies in ZnO ETL possibly can be filled with small and medium-sized anions, such as fluoride, chloride, bromide, and iodide.[52–59] Until now, studies on ZnO doping have focused more on cation doping than on anion doping. Rather, non-excessive oxygen vacancies were expected to help with conductivity enhancement because the oxygen vacancy generally acts as an electron donor in metal oxides. In a study on ZnO ETLs, the relationship between oxygen vacancies and electrical properties has rarely been studied, and little is known about how oxygen vacancies affect the electrical properties of a solution-processed ZnO ETL.

In this study, we have systematically investigated the influence of the cation and anion dopants on the electrical properties of a ZnO ETL through the simultaneous doping of both cations and anions. To investigate the influence of anions, $Al(acac)_3$ (acac = acetylacetonate), $Al(NO_3)_3$, and $AlCl_3$ were introduced as dopants. These three dopants (Cl^-, NO_3^-, $acac^-$) have the same number of different anions together with the same Al cation, thus they provide proper combinations to investigate the effects of different anions. The influence of cations was investigated using NH_4Cl, $AlCl_3$, and $MgCl_2$. In addition, these three dopants (Al^{3+}, Mg^{2+}, NH_4^+) have different numbers of Cl anions, thereby we can collect information about the influence of the number of anions together. To eliminate concerns about the dependence on the photoactive material, the doped ZnO layer was applied on various solar cells fabricated with three different photoactive materials, PTB7-Th:$PC_{71}BM$, PTB7:$PC_{71}BM$, and P3HT:$PC_{71}BM$.

2. Results and discussions

2.1. Optoelectronic properties and morphology

Chemically synthesized nanoparticles or sol–gel driven ZnO thin films are commonly used for the ETL of PCSs. The nanoparticle method allows a lower annealing temperature compared with the sol–gel method, but it is difficult to simultaneously dope cations and anions in ZnO because the anion can be possibly removed during the centrifugal step. Thus, in this work, we prepared doped ZnO by the simple sol–gel method using $Zn(CH_3COO)_2$ in 2-methoxyethanol. The details are provided in the Experimental section.

2.1.1. Electrical properties of ZnO ETL. The resistivity of the ZnO ETL on ITO was characterized by the general 4-point van der Pauw method. The thicknesses of all ZnO samples were approximately 40 nm. The results are summarized in Table 1. Regardless of the type of dopant, whether small or large, doping in all cases led to a decrease in resistivity (increase in conductivity). In the case of same cation Al^{3+}, the resistivity decreased following the decrease of anion diameter ($acac^- > NO^{3-} > Cl^-$). A similar trend is observed in the case of the same anion Cl^-, the resistivity was more decreased with a smaller size of cation dopant ($Al^{3+} < Mg^{2+} < NH_4^+$). Note that, in this case, the cause is not clear because it can also be interpreted as the change in the number of Cl anions. A more interesting point involved the change in the work function by doping. Regardless of the cation, the work function was only changed when the Cl anion was involved. In addition, the work function change was constant regardless of the number of Cl ions.

2.1.2. XPS study. X-ray photoelectron spectroscopy (XPS) was used to characterize the elemental composition and bonding state of ZnO and doped ZnO layers. All samples show similar binding energies of Zn 2p peaks of ~1021.7 eV, ~1044.8 eV and O 1s of ~530.2 eV (Zn–O), ~531.8 eV (Zn–OH), respectively (see Fig. S2 and S3†). This result indicated that the bonding state and crystal structure of ZnO was not changed by doping. In the case of aluminum cation doping, $Al(acac)_3$, $Al(NO_3)_3$, and $AlCl_3$-doped ZnO exhibit Al 2p peaks at 78.39 eV, 78.17 eV and 78.23 eV, respectively (Fig. S4†). The shift of the Al 2p peak toward a higher binding energy compared with Al_2O_3 (note that the Al 2p peak in Al_2O_3 is revealed at ~74.6 eV)[43] indicates the presence of Al^{3+} in the ZnO lattice. The C 1s peak of pristine ZnO and $Al(acac)_3$-doped ZnO are characterized in the energy range of 280–294 eV (Fig. 1a and S5†). Almost identical C 1s features were observed in both pristine ZnO and $Al(acac)_3$-doped ZnO samples at 284.9 eV and 289.3 eV, respectively. The C 1s peaks in pristine ZnO and $Al(acac)_3$-doped ZnO were probably derived from residual acetate, ethanolamine, and acetylacetonate. The ratios of C 1s(C–C, C–H)/C 1s(C=O, C–O) in pristine ZnO and $Al(acac)_3$ doped ZnO were 3.56 and 3.58, respectively. Just a small increase in the C of C–C and C–H indicated that there was a low presence of acetylacetonate in the ZnO layer, which means the influence of acetylacetonate on the ZnO layer seems to be negligible. A slight enhancement of the resistance in $Al(acac)_3$-doped ZnO seems to be mainly due to Al.

For the ZnO layer doped with $Al(NO_3)_3$, the N 1s peak was revealed in the energy range of 390–410 eV (Fig. 1c and S6†). The N 1s signal of $Al(NO_3)_3$-doped ZnO consists of two peaks at 398.5 eV and 406.4 eV, belonging to residual ethanolamine and nitrate, respectively. For the NH_4Cl-doped ZnO, the N 1s peaks were detected at 396.0 eV and 399.0 eV, which were attributed to ammonium and residual ethanolamine, respectively. The XPS spectra of $AlCl_3$-doped ZnO, NH_4Cl-doped ZnO and $MgCl_2$-doped ZnO showed metal chloride-Cl 2p peaks at 198.7 eV,

Table 1 Resistance and work function of different ETLs

Layer	Mean resistance[a] (Ω)	Sheet resistance[a] (Ω per square)	Work function[b] (eV)
ITO/ZnO	1.99 ± 0.14	9.01 ± 0.63	4.03
ITO/ZnO + $Al(acac)_3$	1.85 ± 0.11	8.39 ± 0.50	4.01
ITO/ZnO + $Al(NO_3)_3$	1.58 ± 0.15	7.15 ± 0.68	4.06
ITO/ZnO + $AlCl_3$	1.40 ± 0.12	6.33 ± 0.54	4.30
ITO/ZnO + NH_4Cl	1.68 ± 0.15	7.61 ± 0.67	4.32
ITO/ZnO + $MgCl_2$	1.57 ± 0.11	7.10 ± 0.49	4.35

[a] Mean and sheet resistances were characterized from 4-point measurements on 3 different points. [b] Work functions were characterized from the UPS.

199.0 eV, and 199.0 eV, and nonmetal chloride–Cl 2p peaks at 200.3 eV, 201.0 eV and 201.0 eV, respectively (Fig. 1d–f and S7†). A slight shifting of the Cl 2p peak to a lower binding energy in $AlCl_3$-doped ZnO indicates that $AlCl_3$-doped ZnO has a better metallic property compared with the ZnO doped with NH_4Cl or $MgCl_2$. This result was consistent with the 4-point probe results in Table 1. $AlCl_3$-doped ZnO shows a better conductivity than NH_4Cl-doped ZnO and $MgCl_2$-doped ZnO.

2.1.3. Morphology study. To investigate the effect of doping on the morphology of the ZnO layer, atomic force microscopy (AFM) measurements were carried out, as shown in Fig. 2 (see also Fig. S8†). The pristine ZnO layer and ZnO layers doped with $Al(acac)_3$ or $Al(NO_3)_3$ showed a clear wrinkled structure. For the ZnO layer doped with $AlCl_3$, although the wrinkled structure was substantially blurred, it is still visible. However, such a wrinkled structure was more blurred in the ZnO layer doped

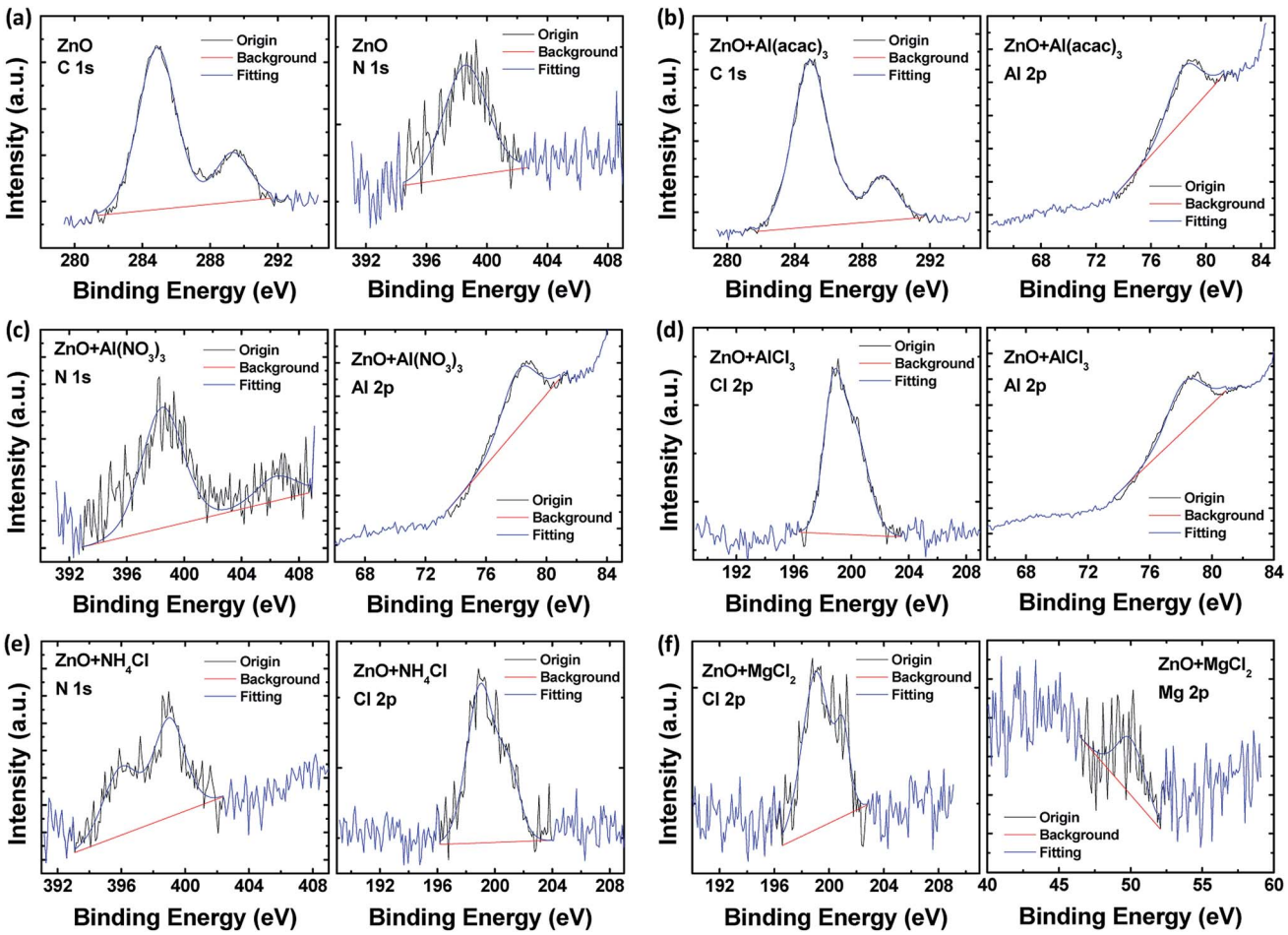

Fig. 1 XPS analysis for the selective elements of doped ZnO. (a) C 1s and N 1s bonds of pristine ZnO, (b) C 1s and Al 2p bonds of $Al(acac)_3$-doped ZnO, (c) N 1s and Al 2p peaks of $Al(NO_3)_3$-doped ZnO, (d) Cl 2p and Al 2p bonds of $AlCl_3$-doped ZnO, (e) N 1s and Cl 2p peaks of NH_4Cl-doped ZnO, (f) Cl 2p and Mg 2p bonds of $MgCl_2$-doped ZnO.

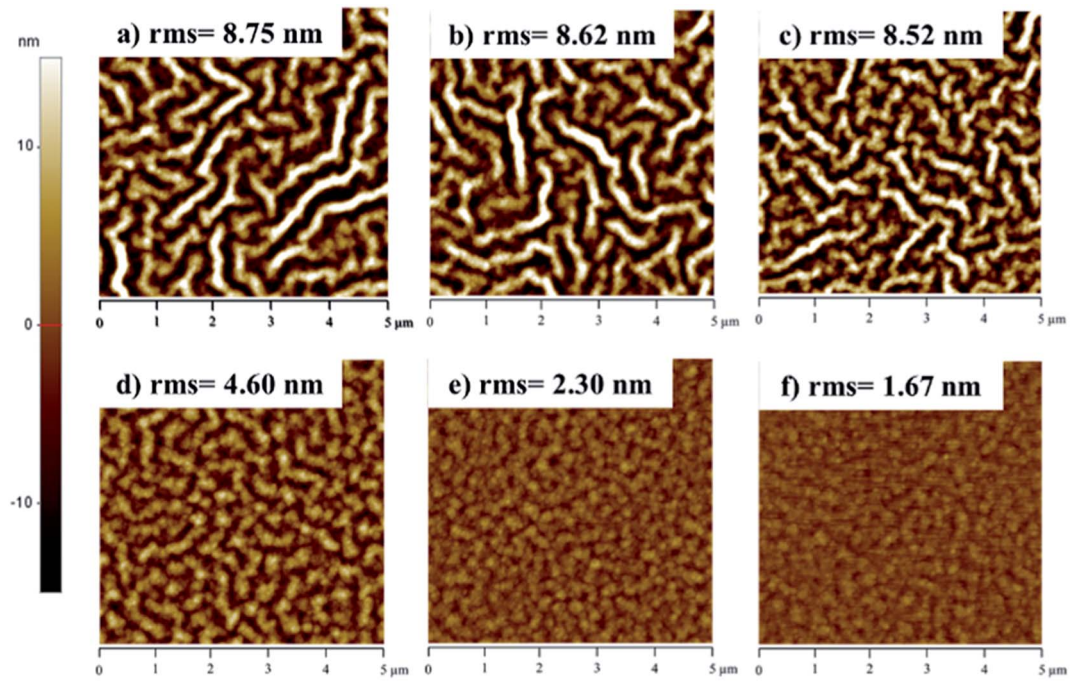

Fig. 2 AFM images of ZnO ETLs. (a) Pristine ZnO, (b) ZnO doped with $Al(acac)_3$, (c) ZnO doped with $Al(NO_3)_3$, (d) ZnO doped with $AlCl_3$, (e) ZnO doped with NH_4Cl, (f) ZnO doped with $MgCl_2$.

with NH_4Cl, and it finally disappeared in the ZnO layer doped with $MgCl_2$.

In comparing the three ZnO films doped with identical cations (Al^{3+}) and different anions (Cl^-, NO_3^-, $acac^-$), the morphology of ZnO doped with $Al(acac)_3$ or $Al(NO_3)_3$ showed a morphology similar to the pristine ZnO ripple. However, the ZnO film doped with $AlCl_3$ showed a relatively homogeneous peak-to-peak structure and smoother surface, with a significantly reduced rms of 4.60 nm. These results clearly indicate that the Cl^- anion affected the ZnO morphology more strongly than $acac^-$ and NO_3^-, which might due to the easier occupation of oxygen vacancies by the smaller Cl^- anion relative to the larger $acac^-$ and NO_3^- anions. Comparing the ZnO films doped with the identical Cl^- anion (Fig. 2d–f), NH_4^+- and Mg^{2+}-doped ZnO films showed a more smooth and flat surface structure with rms values of 2.30 nm and 1.67 nm, respectively. Although the wrinkled structure of ZnO delivered some enhancement of the light absorption *via* light scattering, the current homogeneity can be significantly disturbed at the interface between the photoactive and ZnO layers. Therefore, it is necessary to derive an appropriate optimal point between the morphology change by doping and the improvement of electric characteristics.

2.1.4. Workfunction study. To investigate the influence of dopants on the energy levels of ZnO, ultraviolet photoelectron spectroscopy (UPS) was performed (Table 1 and Fig. S10†). The energy band diagram deduced from the UPS results is shown in Fig. 3. Doped ZnO films with $Al(acac)_3$ and $Al(NO_3)_3$ showed a work function similar to a pristine un-doped ZnO film. With the same Cl^- dopant, $AlCl_3$-, NH_4Cl-, and $MgCl_2$-doped ZnO films showed a ~0.3 eV deeper work function compared to the pristine undoped ZnO film. These results indicate that the low concentration of Al^{3+} did not distort the ZnO polycrystalline structure. The effects of defect occupation by $acac^-$ and NO_3^- were almost negligible. In addition, doping with Mg^{2+} and NH_4^+ also insignificantly affected the work function of the ZnO layer. Only doping with chlorides induced a modification of the work function of the ZnO film by effectively occupying the oxygen vacancies in the ZnO lattice.

2.1.5. Electron mobility and EIS study. Electron mobilities (μ_e) along the vertical direction of the devices were measured using the space charge limited current (SCLC) method, as shown in Fig. 4. A device with a pristine ZnO layer exhibits a μ_e of 5.09×10^{-5} cm^2 V^{-1} s^{-1}. The devices with $Al(acac)_3$, $Al(NO_3)_3$-, $AlCl_3$-, NH_4Cl-, and $MgCl_2$-doped ZnO layers exhibited better electron mobilities of 1.95×10^{-4} cm^2 V^{-1} s^{-1}, 3.05×10^{-4} cm^2 V^{-1} s^{-1}, 6.74×10^{-4} cm^2 V^{-1} s^{-1}, 1.24×10^{-4} cm^2 V^{-1} s^{-1}, and

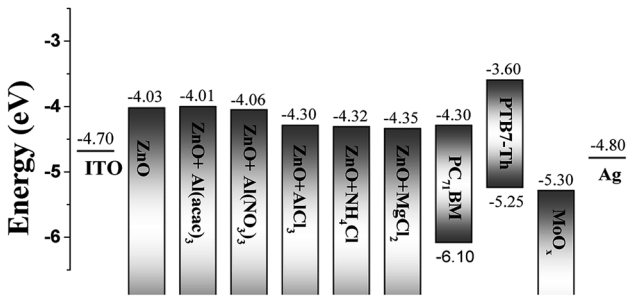

Fig. 3 Energy level diagram of doped ZnO layers obtained from the UPS study. Energy levels of active materials (PTB7-Th, $PC_{71}BM$) and MoO_x hole transport layer are presented together.

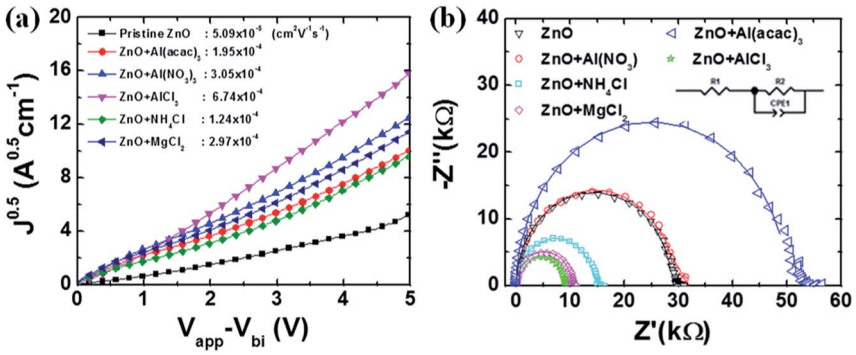

Fig. 4 (a) SCLC characteristics of PTB7-Th:$PC_{71}BM$ electron only devices (device structures: Al/LiF/PTB7-Th:$PC_{71}BM$/ETLs/ITO), (b) Nyquist plots of PTB7-Th:$PC_{71}BM$ with various ETLs.

2.97×10^{-4} cm^2 V^{-1} s^{-1}, respectively. The device with an $AlCl_3$-doped ZnO layer showed the highest μ_e.

Fig. 4b shows the Nyquist plots of impedance spectroscopy (EIS) measurements for PTB7-Th:$PC_{71}BM$ solar cells with pristine ZnO or doped ZnO films measured at open circuit potentials (OCP) under the dark condition. All devices exhibited one semicircle without a transmission line. Series resistances (R_s) and shunt resistances (R_{sh}) are extracted from a fitting line and the results are summarized in Table S1.† In general, a low R_s and high R_{sh} are desired to obtain high-performance solar cells. The device with a pristine ZnO film and the devices with doped ZnO films all perform acceptably with a high R_{sh} of over 5.0 kΩ, which is adequate for solar cells. All doped ZnO devices exhibit a smaller R_s than a pristine undoped ZnO device and among them, the $AlCl_3$-doped ZnO device shows the lowest R_s.

2.2. Photovoltaic performance

2.2.1. The influence of a doped ZnO ETL on the photovoltaic performance. The effects of doped ZnO layers as ETLs on the photovoltaic performance were investigated using three common donor polymers, PTB7-Th, PTB7, and P3HT, all with a $PC_{71}BM$ acceptor. The *J–V* characteristics of PTB7-Th devices with various ETLs are exhibited in Fig. 5a and b and the photovoltaic parameters are summarized in Table 2. The control PSC with a pristine ZnO ETL gives a PCE of 9.16%, which is similar to previous reports.[35,36] In comparison within different anion/same Al cation groups ($Al(acac)_3$, $Al(NO_3)_3$, $AlCl_3$), the devices with $Al(acac)_3$- or $Al(NO_3)_3$-doped ZnO ETLs showed enhanced PCEs of 9.71% and 9.79%, respectively. An even more enhanced PCE was observed in the solar cell with an

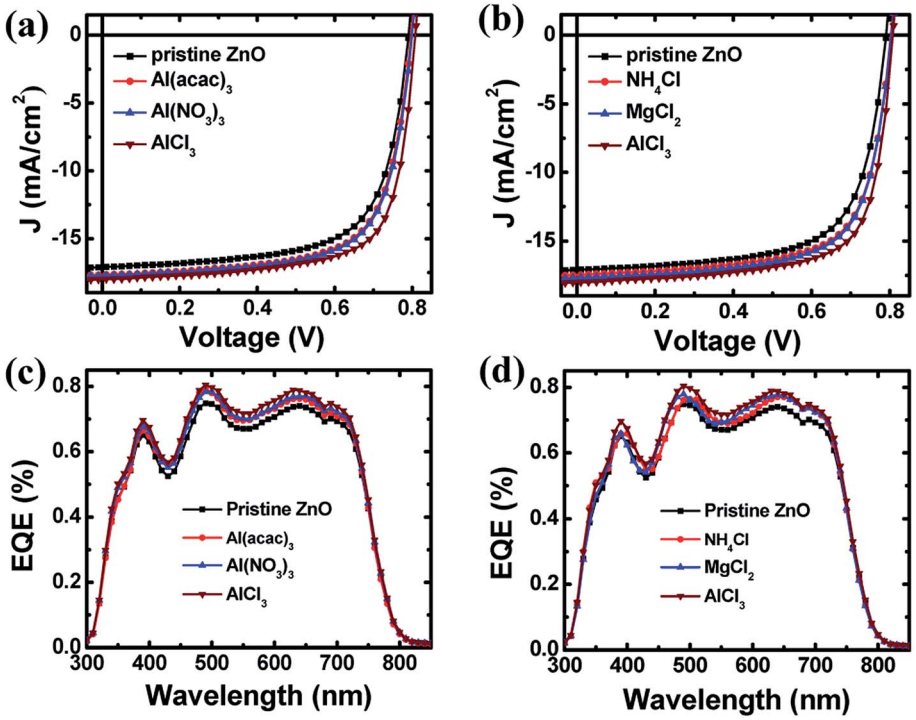

Fig. 5 (a and b) *J–V* curves and (c and d) EQE spectra of devices with different electron transporting layers.

Table 2 Photovoltaic performances of the solar cells under AM 1.5G illumination at 100 mW cm^{-2} with different electron transporting layers

ETL	PCE best (%)	PCE avg.[a] (%)	FF (%)	V_{oc} (V)	J_{sc} (mA cm^{-2})	J_{sc} [b] (mA cm^{-2})	R_s [c] (Ω)
ZnO	9.16	8.89	67.7	0.790	17.10	16.57	32.8
ZnO + $Al(acac)_3$	9.71	9.44	68.8	0.796	17.68	17.15	25.8
ZnO + $Al(NO_3)_3$	9.79	9.57	69.0	0.799	17.74	17.32	26.5
ZnO + $AlCl_3$	10.38	10.15	71.3	0.807	18.01	17.64	22.4
ZnO + NH_4Cl	9.73	9.43	69.3	0.802	17.47	17.09	28.0
ZnO + $MgCl_2$	9.83	9.68	69.1	0.803	17.70	17.23	28.2
ZnO/PEIE[d]	10.14	9.76	70.2	0.804	17.94		26.1
ZnO + $AlCl_3$/PEIE[d]	10.48	10.18	71.8	0.809	18.03		25.8

[a] The average PCE from more than 12 devices. [b] Calculated J_{sc} from EQE spectra. [c] Extraction from solar simulation program. [d] Surface modifying ETLs with PEIE.

$AlCl_3$-doped ZnO layer. The best efficiency of the device with an $AlCl_3$-doped ZnO layer was 10.38%. These results clearly indicate that the Cl dopant exhibited more dominant effects on the photovoltaic performance than acac or NO_3 dopants. However, when comparing the devices with ZnO layers doped with NH_4Cl, $AlCl_3$, or $MgCl_2$, even though NH_4Cl and $MgCl_2$ have the same Cl dopant, the measured PCEs were relatively lower than that of a device with an $AlCl_3$-doped ZnO layer. This result indicated that the Al^{3+} dopant has a better effect on the photovoltaic performance than NH_4^+ or Mg^{2+} dopants.

Consequently, the combination of Al^{3+} and Cl^- dopants boost the doping effect, thereby enhancing the PCE from 9.16% to 10.38%. In the case of solar cells based on P3HT or PTB7 as a donor polymer, the highest PCE was also obtained in the PSC with an $AlCl_3$-doped ZnO ETL, as shown in Fig. S12, S13, Table S2 and S3.† Note that optimization details for a proper $AlCl_3$ doping concentration and an optimal thickness of the $AlCl_3$-doped ZnO ETL are presented in Fig. S14 and S15.† The optimal doping concentration and thickness are 2.5 mM and ~120 nm, respectively.

In our solar cells results, all the solar cell parameters such as J_{sc}, FF, and V_{oc} were improved with doped ZnO. The increase in J_{sc} was considered to be a result of the improvement of the charge transport property of the doped ZnO ETL (Fig. 4a). In case of FF, it might be attributed to reduced charge recombination and reduced resistance (Fig. 4b). For the V_{oc}, slightly increase open circuit voltage was observed with doped ZnO ETL because of Fermi level shift. Generally, V_{oc} change is also related to the photon energy loss. Therefore, higher V_{oc} of the device with doped ZnO ETL was attributed to the reduction of both interfacial recombination and energy loss.

2.2.2. The influence of a doped ZnO ETL on exciton generation. A maximum exciton generation rate (G_{max}) can be obtained following the equation: $J_{sat} = qLG_{max}$, where q is the electron charge and L is the thickness of the active layer.[60] The photocurrent density (J_{ph}) plots as a function of the effective voltage (V_{eff}) are shown in Fig. S16.† The saturation photocurrent densities (J_{sat}) of pristine ZnO, $Al(acac)_3$-doped ZnO, $Al(NO_3)_3$-doped ZnO, $AlCl_3$-doped ZnO, NH_4Cl-doped ZnO, and $MgCl_2$-doped ZnO are 178.1 A m^{-2}, 183.7 A m^{-2}, 184.3 A m^{-2}, 187.2 A m^{-2}, 184.2 A m^{-2}, and 185.5 A m^{-2}, respectively. It is known that the interfacial interaction between an ETL and the active layer is one of the factors that can influence the value of G_{max}. A high G_{max} acts to reduce the recombination at the interface of the ETL and active layer. The calculated G_{max} values of pristine ZnO, $Al(acac)_3$-doped ZnO, $Al(NO_3)_3$-doped ZnO, $AlCl_3$-doped ZnO, NH_4Cl-doped ZnO, and $MgCl_2$-doped ZnO are 9.28×10^{27} m^{-3} s^{-1}, 9.57×10^{27} m^{-3} s^{-1}, 9.60×10^{27} m^{-3} s^{-1}, 9.75×10^{27} m^{-3} s^{-1}, 9.59×10^{27} m^{-3} s^{-1}, and 9.66×10^{27} m^{-3} s^{-1}, respectively, which are consistent with the J_{sc} values of the devices.

2.2.3. External quantum efficiency. The external quantum efficiency (EQE) spectra of devices with pristine ZnO and doped ZnO ETLs are shown in Fig. 5c and d. The EQE spectra of the devices have maximum efficiencies of 75%, 79%, 78%, 80%, 76%, and 78% for ZnO, $Al(acac)_3$-doped ZnO, $Al(NO_3)_3$-doped ZnO, $AlCl_3$-doped ZnO, NH_4Cl-doped ZnO, and $MgCl_2$-doped ZnO, respectively. The integral current density values calculated from the EQE spectra of all devices agree well with the J_{sc} values obtained from the J–V curves (maximum error < 3%).

2.2.4. Stability study. The stability of a PSC is a crucial factor for commercialized applications. It is a well-known fact that defects of ZnO cause a reduction in the long-term stability of inverted PSCs. Fig. 6 shows the long-term stabilities of PSCs with pristine ZnO ETLs and doped ZnO ETLs. The results

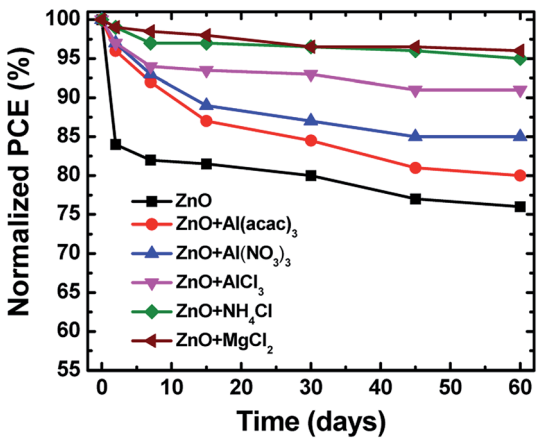

Fig. 6 Normalized PCEs of devices with different ETLs as a function of time monitored in an ambient atmosphere under the dark condition.

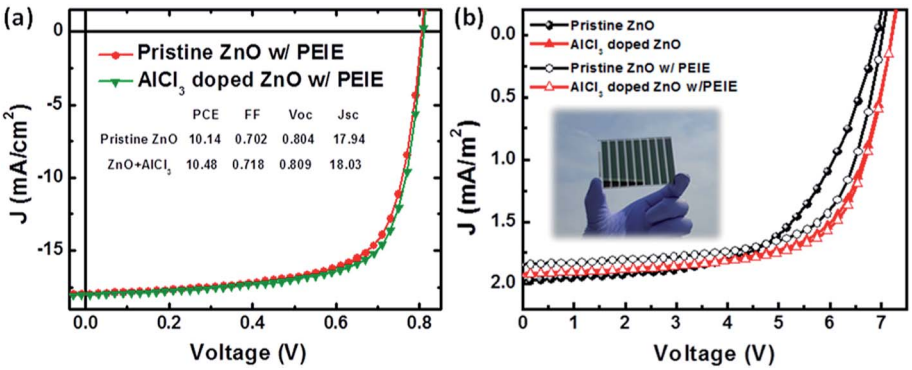

Fig. 7 (a) J–V curves of unit cells with PEIE-modified pristine ZnO and an $AlCl_3$-doped ZnO layer, (b) J–V curves of module devices with PEIE-modified pristine ZnO and $AlCl_3$-doped ZnO.

unambiguously reveal that PSCs with doped ZnO ETLs show better stability than that of the pristine ZnO ETL. Particularly, solar cells with a ZnO layer doped with Cl dopant exhibited better stability. This was attributed to the fact that Cl^- fills the defects of a ZnO layer more efficiently. Although the efficiency was high in the device with an $AlCl_3$-doped ZnO layer, the stability was better in devices with an $MgCl_2$- or NH_4Cl-doped ZnO layer because the similar charge of Mg^{2+} and Zn^{2+} help to minimize the local charge in the ZnO lattice.

2.2.5. Further modification of $AlCl_3$ doped ZnO surface. As a final step, for further modification of the ZnO surface, we employed polyethylenimine ethoxylated (PEIE) to modify the ZnO ripple surface. PEIE is a well-known interfacial organic material, which can enhance the PCE by modifying the ETL surface in inverted PSCs.[61,62] Fig. 7a shows the J–V characteristics of PSCs with pristine ZnO and $AlCl_3$-doped ZnO ETLs, both with surfaces modified by PEIE. The PCE of the pristine ZnO ETL device significantly improved from 9.16% to 10.14% after spin-coating a PEIE layer. In the case of the $AlCl_3$-doped ZnO ETL, the PCE also increased from 10.38% (average PCE of 10.15%) to 10.48% (average PCE of 10.18%). However, the relative increase was smaller than that of pristine ZnO. This is probably because the quality of ZnO itself is already considerably improved by the doping process.

2.2.6. High-performance module device with a doped ZnO layer. Fig. 7b and Table 3 show the performances of inverted organic photovoltaic mini-modules with different electron transporting layers. The OPV module with a ZnO ETL yielded a PCE of 8.00%, with an FF of 58.7%, V_{oc} of 6.914 V, and J_{sc} of 1.973 mA cm^{-2}. On the other hand, the module device with an $AlCl_3$-doped ZnO ETL showed an enhanced PCE of 9.34% with FF = 66.4%, V_{oc} = 7.213 V, and J_{sc} = 1.950 mA cm^{-2}. The module with an $AlCl_3$-doped ZnO ETL showed an improvement of the series resistance (R_S) and FF compared with the ZnO ETL module. To further enhance the performance of the ZnO ETL module, PEIE was additionally employed and resulted in enhanced performance, especially for the FF and R_S. For the module with an $AlCl_3$-doped ZnO ETL, however, we obtained almost similar results before employing PEIE, which is commensurate with the previous cell results.

Table 3 Photovoltaic parameters of the module devices with different electron transporting layers

ETL	PCE (%)	FF (%)	V_{oc} (V)	J_{sc} (mA cm^{-2})	R_s (ohm)
ZnO	8.00	58.7	6.914	1.973	35.688
ZnO + $AlCl_3$	9.34	66.4	7.213	1.950	24.319
ZnO/PEIE	8.66	66.9	7.027	1.843	22.818
ZnO + $AlCl_3$/PEIE	9.36	67.6	7.207	1.922	21.965

3. Conclusions

We have successfully demonstrated an enhanced PCE of inverted solar cells by introducing a doped ZnO electron transport layer. Because of the synergistic effect of dual Al^{3+} and Cl^- doping in the ZnO layer, the photovoltaic efficiency of inverted PSCs were significantly enhanced from 9.16% (with a pristine ZnO layer) to 10.48% (together with PEIE). The role of Al^{3+} was tied to the improvement of conductivity and electron mobility of ZnO. Meanwhile, Cl^- induced the elimination of defects and a reduction in the work function, thereby improving the conductivity, electron mobility, and surface morphology. Comparing the various possible dopant utilized in this study, Al^{3+} shows better optoelectronic properties compared with other larger cations (Mg^{2+}, NH_4^+ and Cl^-) also allows better optoelectronic properties compared with other larger anions (NO_3^-, $acac^-$). Consequently, the combination of Al^{3+} and Cl-dopants boost the doping effect, thereby enhancing the PCE.

4. Experimental section

4.1. Materials and device fabrication

The polymer PTB7-Th (code PCE-10), polymer PTB7, polymer P3HT and $PC_{71}BM$ (purity >99% by HPLC) were purchased from 1-material and utilized without further purification. The high-grade doping precursors, $Al(acac)_3$, $Al(NO_3)_3 \cdot 9H_2O$, $AlCl_3 \cdot 6H_2O$, NH_4Cl, $MgCl_2$, and other chemicals and solvents were purchased from Sigma Aldrich. The sol–gel ZnO precursor solution (0.5 M) was prepared using $Zn(CH_3COOH)_2 \cdot 2H_2O$ (1.09 g, 5 mmol) and 2-ethanolamine (500 μL) were dissolved in

2-methoxyethanol (10 mL). The solution was stirred at 60 °C for 2 hours then filtered using a 0.2 μm PTFE filter. Similar to the ZnO precursor solution, the sol–gel doped ZnO precursor solutions were obtained by adding salt sources ($Al(acac)_3$: 2.5 mM, $Al(NO_3)_3$: 2.5 mM, $AlCl_3$: 2.5 mM, NH_4Cl: 7.5 mM, $MgCl_2$: 3.7 mM) together with $Zn(CH_3COO)_2 \cdot 2H_2O$ into 2-methoxyethanol. A 0.05% w/w PEIE solution was prepared with anhydrous ethanol. Solutions of PTB7-Th : $PC_{71}BM$ (1.0 : 1.5 wt) or PTB7 : $PC_{71}BM$ (1.0 : 1.5 wt), both with a total concentration of 20 mg mL^{-1}, were dissolved in chlorobenzene : 1,8-diiodooctane (97 : 3 v/v) and stirred at 70 °C overnight. P3HT : $PC_{71}BM$ (1.0 : 0.8 wt), with a total concentration of 40 mg mL^{-1} dissolved in 1,2-dichlorobenzene (ODCB). Then solutions were filtered through a 0.45 μm pore size PTFE and stored in an Argon-filled glovebox.

Inverted polymer solar cells were fabricated by spin-coating ZnO or the doped ZnO precursor on the UV-pretreated ITO (140 nm, 15 Ω sq^{-1}) and annealing at 180 °C in air for 10 minutes to form a ~50 nm thick ZnO layer. In the case using PEIE as a surface-modified layer, the PEIE solution was spun at 3000 rpm on the ZnO layers and then annealed at 100 °C in air for 10 minutes. The devices were transferred into the glovebox for spin-coating the active layer with controlled thickness. The active layer thicknesses of PTB7-Th:$PC_{71}BM$, PTB7:$PC_{71}BM$ and P3HT:$PC_{71}BM$ were 120 ± 5 nm, 100 ± 5 nm and 240 ± 8 nm, respectively. In the case of P3HT, devices were annealed at 140 °C for 10 minutes. The resulting devices were then dried under high vacuum ($<5 \times 10^{-6}$ mbar) for 3 hours. Finally, MoO_3 (5 nm) and Ag (100 nm) electrodes were sequentially deposited on the active layer through a shadow mask by thermal evaporation ($<5 \times 10^{-6}$ mbar), which defines the active area of 0.13 cm^2. Module devices for out-of-lab testing were fabricated with the same procedures as described in the unit cell fabrication. The areas of the photoactive layers were 18.63 cm^2. A module consists of a monolithic interconnection of individual stripe pattern sub-cells in series by covering the negative contact of one ITO substrate with the positive contact of the lateral top electrode.

4.2. Device characterization

The *J–V* curves of devices were characterized using a Keithley 2400 source with MODUSYS solar simulator (PS-KS2C) under AM 1.5G simulated illumination (100 mW cm^{-2}). The EQE spectra were characterized using a QE/IPCE/spectra response measurement system (ABET Technologies). The resistance/square of ITO and ITO/ETLs were characterized by a 4-point probe set (MODUSYS). The transmittance spectra were measured using a UV-vis spectrometer (Varian Co., Carry 5000 model). Ultraviolet photoelectron spectroscopy (UPS) measurements of ITO/ETLs were carried out by a Multilab-2000 (Thermo Scientific) instrument using He I photons ($h\nu = 21.22$ eV). X-ray photoelectron spectroscopy (XPS) measurements of the Si wafer/ETLs were carried out by the same instrument, with the UPS using monochromatized Al Kα X-ray photons ($h\nu = 1486.6$ eV). Atomic force microscopy (AFM) measurements of ITO/ETLs were performed by a Dimension Icon Scanning Probe Microscope (Bruker). The electrochemical impedance spectroscopy (EIS) measurements were performed on a ZIVE SP5 (ZIVE LAB, Korea) in the frequency range from 1 MHz to 1 Hz, with a perturbation amplitude of 0.1 V. The impedance spectra were characterized at their open-circuit potentials (OCP) under the dark condition.

To characterize the vertical electron mobility, a space charge limited current (SCLC) model was applied. The device structures of Al (100 nm)/LiF (0.5 nm)/PTB7-Th:$PC_{71}BM$ (120 nm)/ZnO or doped ZnO (40 nm)/ITO were used and *J–V* curves over the range 0–5 V were characterized in the dark condition. The electron mobilities were calculated using the SCLC model, where the SCLC is described by $J = 9\varepsilon_0\varepsilon_r\mu V^2/8L^3$, where J is the current density, L is the film thickness of the active layer, μ is the electron mobility, ε_r is the relative dielectric constant of the transport medium, ε_0 is the permittivity of free space (8.85×10^{-12} F m^{-1}), V is the internal voltage in the device, and $V = V_{appl} - V_{bi}$, where V_{appl} is the applied voltage to the device and V_{bi} is the built-in voltage due to the relative work function difference of the two electrodes.

Author contributions

S. K., A. P., M. J. and Q. V. H. designed the fabricated solar cells and conducted the characterization. S. K., S. C. and D. C. L. wrote the manuscript. J. H. J. and Q. V. H. provided supporting materials and contacted the analysis center. J. W. H. and Y. H. K. gave valuable suggestions during the writing of the manuscript. D. C. L. supervised the whole project. All authors discussed the results and commented on the manuscript.

Conflicts of interest

The authors declare no competing financial interests.

Acknowledgements

This research was mainly supported by a grant from the Korea Institute of Materials Science (KIMS) and the Korea Institute of Energy Technology Evaluation and Planning (KETEP, No. 20173030014180, No. 2018201010636A). The portion of this research conducted at the University of Ulsan was supported by a National Research Foundation of Korea grant (2017R1A2B4003583, 2017M2A2A6A01018599, 2019R1A6A1A11053838).

References

1 C. J. Brabec, N. S. Sariciftci and J. C. Hummelen, *Adv. Funct. Mater.*, 2001, **11**, 15–26.
2 C. Wang, C. Li, R. C. I. Mackenzie, S. Wen, Y. Liu, P. Ma, G. Wang, W. Tian and S. Ruan, *J. Mater. Chem. A*, 2018, **6**, 17662–17670.
3 J. Subbiah, V. D. Mitchell, N. K. C. Hui, D. J. Jones and W. W. H. Wong, *Angew. Chem., Int. Ed.*, 2017, **56**, 8431–8434.
4 G. Li, R. Zhu and Y. Yang, *Nat. Photonics*, 2012, **6**, 153–161.

5 J. Yuan, Y. Zhang, L. Zhou, G. Zhang, H.-L. Yip, T.-K. Lau, X. Lu, C. Zhu, H. Peng, P. A. Johnson, M. Leclerc, Y. Cao, J. Ulanski, Y. Li and Y. Zou, *Joule*, 2019, **3**, 1140–1151.
6 Y. Cui, H. Yao, J. Zhang, T. Zhang, Y. Wang, L. Hong, K. Xian, B. Xu, S. Zhang, J. Peng, Z. Wei, F. Gao and J. Hou, *Nat. Commun.*, 2019, **10**, 1–8.
7 V. Gupta, A. K. K. Kyaw, D. H. Wang, S. Chand, G. C. Bazan and A. J. Heeger, *Sci. Rep.*, 2013, **3**, 1965.
8 C. Y. Jiang, X. W. Sun, D. W. Zhao, A. K. K. Kyaw and Y. N. Li, *Sol. Energy Mater. Sol. Cells*, 2010, **94**, 1618–1621.
9 H.-L. Yip, S. K. Hau, N. S. Baek, H. Ma and A. K. Y. Jen, *Adv. Mater.*, 2008, **20**, 2376–2382.
10 D. W. Zhao, P. Liu, X. W. Sun, S. T. Tan, L. Ke and A. K. K. Kyaw, *Appl. Phys. Lett.*, 2009, **95**, 153304.
11 X. Bulliard, S.-G. Ihn, S. Yun, Y. Kim, D. Choi, J.-Y. Choi, M. Kim, M. Sim, J.-H. Park, W. Choi and K. Cho, *Adv. Funct. Mater.*, 2010, **20**, 4381–4387.
12 J. Huang, Z. Yin and Q. Zheng, *Energy Environ. Sci.*, 2011, **4**, 3861–3877.
13 Z. Liang, Q. Zhang, O. Wiranwetchayan, J. Xi, Z. Yang, K. Park, C. Li and G. Cao, *Adv. Funct. Mater.*, 2012, **22**, 2194–2201.
14 K.-D. Kim, D. C. Lim, J. Hu, J.-D. Kwon, M.-G. Jeong, H. O. Seo, J. Y. Lee, K.-Y. Jang, J.-H. Lim, K. H. Lee, Y. Jeong, Y. D. Kim and S. Cho, *ACS Appl. Mater. Interfaces*, 2013, **5**, 8718–8723.
15 S. Nho, G. Baek, S. Park, B. R. Lee, M. J. Cha, D. C. Lim, J. H. Seo, S.-H. Oh, M. H. Song and S. Cho, *Energy Environ. Sci.*, 2016, **9**, 240–246.
16 K. Lee, J. Y. Kim, S. H. Park, S. H. Kim, S. Cho and A. J. Heeger, *Adv. Mater.*, 2007, **19**, 2445–2449.
17 S. H. Park, A. Roy, S. Beaupre, S. Cho, N. Coates, J. S. Moon, D. Moses, M. Leclerc, K. Lee and A. J. Heeger, *Nat. Photonics*, 2009, **3**, 297–302.
18 X. Bao, L. Sun, W. Shen, C. Yang, W. Chen and R. Yang, *J. Mater. Chem. A*, 2014, **2**, 1732–1737.
19 S. Trost, K. Zilberberg, A. Behrendt and T. Riedl, *J. Mater. Chem.*, 2012, **22**, 16224–16229.
20 B. Bob, T.-B. Song, C.-C. Chen, Z. Xu and Y. Yang, *Chem. Mater.*, 2013, **25**, 4725–4730.
21 S. Trost, A. Behrendt, T. Becker, A. Polywka, P. Görrn and T. Riedl, *Adv. Energy Mater.*, 2015, **5**, 1500277.
22 Z. a. Tan, S. Li, F. Wang, D. Qian, J. Lin, J. Hou and Y. Li, *Sci. Rep.*, 2014, **4**, 4691.
23 H. Fan and X. Zhu, *ACS Appl. Mater. Interfaces*, 2016, **8**, 33856–33862.
24 J. J. Jasieniak, J. Seifter, J. Jo, T. Mates and A. J. Heeger, *Adv. Funct. Mater.*, 2012, **22**, 2594–2605.
25 B. J. Tremolet de Villers, R. C. I. MacKenzie, J. J. Jasieniak, N. D. Treat and M. L. Chabinyc, *Adv. Energy Mater.*, 2014, **4**, 1301290.
26 F. Xie, W. C. H. Choy, C. Wang, X. Li, S. Zhang and J. Hou, *Adv. Mater.*, 2013, **25**, 2051–2055.
27 K. Zilberberg, S. Trost, J. Meyer, A. Kahn, A. Behrendt, D. Lützenkirchen-Hecht, R. Frahm and T. Riedl, *Adv. Funct. Mater.*, 2011, **21**, 4776–4783.
28 G. Teran-Escobar, J. Pampel, J. M. Caicedo and M. Lira-Cantu, *Energy Environ. Sci.*, 2013, **6**, 3088–3098.
29 S. Bai, M. Cao, Y. Jin, X. Dai, X. Liang, Z. Ye, M. Li, J. Cheng, X. Xiao, Z. Wu, Z. Xia, B. Sun, E. Wang, Y. Mo, F. Gao and F. Zhang, *Adv. Energy Mater.*, 2014, **4**, 1301460.
30 F. Jiang, W. C. H. Choy, X. Li, D. Zhang and J. Cheng, *Adv. Mater.*, 2015, **27**, 2930–2937.
31 T. Stubhan, N. Li, N. A. Luechinger, S. C. Halim, G. J. Matt and C. J. Brabec, *Adv. Energy Mater.*, 2012, **2**, 1433–1438.
32 M. Vasilopoulou, A. Soultati, D. G. Georgiadou, T. Stergiopoulos, L. C. Palilis, S. Kennou, N. A. Stathopoulos, D. Davazoglou and P. Argitis, *J. Mater. Chem. A*, 2014, **2**, 1738–1749.
33 M. Jørgensen, K. Norrman and F. C. Krebs, *Sol. Energy Mater. Sol. Cells*, 2008, **92**, 686–714.
34 Z. Yin and Q. Zheng, *Adv. Energy Mater.*, 2012, **2**, 179–218.
35 Z. Yin, J. Wei and Q. Zheng, *Adv. Sci.*, 2016, **3**, 1500362.
36 Z. Liang, Q. Zhang, L. Jiang and G. Cao, *Energy Environ. Sci.*, 2015, **8**, 3442–3476.
37 W. Zhongwei, S. Tao, X. Zhouhui, W. Huaixin and S. Baoquan, *Nanotechnology*, 2013, **24**, 484012.
38 T. Stubhan, M. Salinas, A. Ebel, F. C. Krebs, A. Hirsch, M. Halik and C. J. Brabec, *Adv. Energy Mater.*, 2012, **2**, 532–535.
39 J. Jo, J.-R. Pouliot, D. Wynands, S. D. Collins, J. Y. Kim, T. L. Nguyen, H. Y. Woo, Y. Sun, M. Leclerc and A. J. Heeger, *Adv. Mater.*, 2013, **25**, 4783–4788.
40 S. Shao, K. Zheng, T. Pullerits and F. Zhang, *ACS Appl. Mater. Interfaces*, 2013, **5**, 380–385.
41 C.-H. Hsieh, Y.-J. Cheng, P.-J. Li, C.-H. Chen, M. Dubosc, R.-M. Liang and C.-S. Hsu, *J. Am. Chem. Soc*, 2010, **132**, 4887–4893.
42 S.-H. Liao, H.-J. Jhuo, Y.-S. Cheng and S.-A. Chen, *Adv. Mater.*, 2013, **25**, 4766–4771.
43 L. K. Jagadamma, M. Al-Senani, A. El-Labban, I. Gereige, G. O. Ngongang Ndjawa, J. C. D. Faria, T. Kim, K. Zhao, F. Cruciani, D. H. Anjum, M. A. McLachlan, P. M. Beaujuge and A. Amassian, *Adv. Energy Mater.*, 2015, **5**, 1500204.
44 X. Liu, X. Li, Y. Li, C. Song, L. Zhu, W. Zhang, H.-Q. Wang and J. Fang, *Adv. Mater.*, 2016, **28**, 7405–7412.
45 A. Puetz, T. Stubhan, M. Reinhard, O. Loesch, E. Hammarberg, S. Wolf, C. Feldmann, H. Kalt, A. Colsmann and U. Lemmer, *Sol. Energy Mater. Sol. Cells*, 2011, **95**, 579–585.
46 Z. Yin, Q. Zheng, S.-C. Chen, D. Cai and Y. Ma, *Adv. Energy Mater.*, 2016, **6**, 1501494.
47 J. Jae Hoon, H. Kihyon, K. Se-Hun and L. Dong Chan, *J. Korean Inst. Surf. Eng.*, 2016, **49**, 490–497.
48 E. Polydorou, I. Sakellis, A. Soultati, A. Kaltzoglou, T. A. Papadopoulos, J. Briscoe, D. Tsikritzis, M. Fakis, L. C. Palilis, S. Kennou, P. Argitis, P. Falaras, D. Davazoglou and M. Vasilopoulou, *Nano Energy*, 2017, **34**, 500–514.
49 Q. Zhu, X. Bao, J. Yu, D. Zhu, Q. Zhang, C. Gu, H. Dong, R. Yang and L. Dong, *Thin Solid Films*, 2016, **605**, 202–207.
50 R. Shannon, *Acta Crystallogr., Sect. A: Cryst. Phys., Diffr., Theor. Gen. Crystallogr.*, 1976, **32**, 751–767.

51 A. A. Al-Ghamdi, O. A. Al-Hartomy, M. El Okr, A. M. Nawar, S. El-Gazzar, F. El-Tantawy and F. Yakuphanoglu, *Spectrochim. Acta, Part A*, 2014, **131**, 512–517.
52 J. Hu and R. G. Gordon, *Sol. Cells*, 1991, **30**, 437–450.
53 F. Wang, J.-H. Seo, Z. Li, A. V. Kvit, Z. Ma and X. Wang, *ACS Appl. Mater. Interfaces*, 2014, **6**, 1288–1293.
54 Y. Zhang, C. Liu, J. Liu, J. Xiong, J. Liu, K. Zhang, Y. Liu, M. Peng, A. Yu, A. Zhang, Y. Zhang, Z. Wang, J. Zhai and Z. L. Wang, *ACS Appl. Mater. Interfaces*, 2016, **8**, 1381–1387.
55 W.-Q. Wu, Q. Wang, Y. Fang, Y. Shao, S. Tang, Y. Deng, H. Lu, Y. Liu, T. Li, Z. Yang, A. Gruverman and J. Huang, *Nat. Commun.*, 2018, **9**, 1625.
56 W. Q. Wu, J. F. Liao, Y. Jiang, L. Wang and D. B. Kuang, *Small*, 2019, **15**, 1900606.
57 J.-F. Liao, W.-Q. Wu, J.-X. Zhong, Y. Jiang, L. Wang and D.-B. Kuang, *J. Mater. Chem. A*, 2019, **7**, 9025–9033.
58 M. J. Kim and T. G. Kim, *ACS Appl. Mater. Interfaces*, 2016, **8**, 5453–5457.
59 C. A. Hoel, T. O. Mason, J.-F. Gaillard and K. R. Poeppelmeier, *Chem. Mater.*, 2010, **22**, 3569–3579.
60 Q. V. Hoang, C. E. Song, I.-N. Kang, S.-J. Moon, S. K. Lee, J.-C. Lee and W. S. Shin, *RSC Adv.*, 2016, **6**, 28658–28665.
61 A. K. K. Kyaw, D. H. Wang, V. Gupta, J. Zhang, S. Chand, G. C. Bazan and A. J. Heeger, *Adv. Mater.*, 2013, **25**, 2397–2402.
62 B. A. E. Courtright and S. A. Jenekhe, *ACS Appl. Mater. Interfaces*, 2015, **7**, 26167–26175.